

PAPER

Structural and practical identifiability of dual-input kinetic modeling in dynamic PET of liver inflammation

To cite this article: Yang Zuo *et al* 2019 *Phys. Med. Biol.* **64** 175023

View the [article online](#) for updates and enhancements.

You may also like

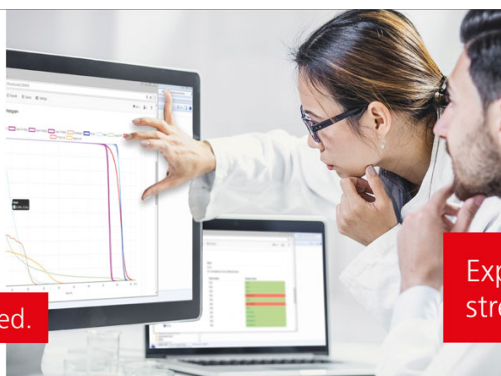
- [Nonlinear Identifiability Analysis of the Porous Electrode Theory Model of Lithium-Ion Batteries](#)
Marc D. Berliner, Hongbo Zhao, Supratim Das *et al.*
- [Experimental Parameter Identification of a LiFePO₄ Thermal Battery Model through Identifiability Maximization Using Input Trajectory Optimization](#)
Sergio Mendoza, Michael Rothenberger, Alison Hake *et al.*
- [Practical identifiability of mathematical models of biomedical processes](#)
Sergey Kabanikhin, Maktagali Bektemesov, Olga Krivorotko *et al.*

VERIQA

RT MonteCarlo 3D

Plan selected. Plan verified.
In less than 3 minutes.

Automated. Independent. Web-Based.



PTW THE
DOSIMETRY
COMPANY

Explore the benefits of
streamlined patient QA



PAPER

Structural and practical identifiability of dual-input kinetic modeling in dynamic PET of liver inflammation

Yang Zuo¹, Souvik Sarkar², Michael T Corwin¹, Kristin Olson³, Ramsey D Badawi¹ and Guobao Wang^{1,4} ¹ Department of Radiology, University of California at Davis, Sacramento, CA 95817, United States of America² Department of Internal Medicine, University of California at Davis, Sacramento, CA 95817, United States of America³ Department of Pathology and Laboratory Medicine, University of California at Davis, Sacramento, CA 95817, United States of America⁴ Author to whom any correspondence should be addressed.E-mail: gbwang@ucdavis.edu**Keywords:** liver inflammation, dynamic PET, dual-input kinetic modeling, structural identifiability, practical identifiability**Abstract**

Dynamic ¹⁸F-FDG PET with tracer kinetic modeling has the potential to noninvasively evaluate human liver inflammation using the FDG blood-to-tissue transport rate K_1 . Accurate kinetic modeling of dynamic liver PET data and K_1 quantification requires the knowledge of dual-blood input function from the hepatic artery and portal vein. While the arterial input function can be derived from the aortic region on dynamic PET images, it is difficult to extract the portal vein input function accurately from PET images. The optimization-derived dual-input kinetic modeling approach has been proposed to overcome this problem by jointly estimating the portal vein input function and FDG tracer kinetics from time activity curve fitting. In this paper, we further characterize the model properties by analyzing the structural identifiability of the model parameters using the Laplace transform and practical identifiability using computer simulation based on fourteen patient datasets. The theoretical analysis has indicated that all the kinetic parameters of the dual-input kinetic model are structurally identifiable, though subject to local solutions. The computer simulation results have shown that FDG K_1 can be estimated reliably in the whole-liver region of interest with reasonable bias, standard deviation, and high correlation between estimated and original values, indicating of practical identifiability of K_1 . The result has also demonstrated the correlation between K_1 and histological liver inflammation scores is reliable. FDG K_1 quantification by the optimization-derived dual-input kinetic model is promising for assessing liver inflammation.

1. Introduction

Nonalcoholic steatohepatitis (NASH) is a progressive nonalcoholic fatty liver disease (NAFLD) affecting approximately 5–10 million patients in the United States (Musso *et al* 2011, Michelotti *et al* 2013). The hallmark of NASH is hepatic inflammation and injury in the setting of hepatic steatosis (Wree *et al* 2013). Clinical assessment of liver inflammation can only be made by invasive liver biopsy (Lee and Park 2014). There is currently no effective noninvasive imaging method in the clinic. PET imaging of translocator protein (TSPO) has shown some promise in small-animal studies (Xie *et al* 2012). Its translation and adoption as a clinical tool, however, is likely to take time. On the other hand, ¹⁸F-fluorodeoxyglucose positron emission tomography (FDG-PET) is widely accessible in clinics. While static FDG-PET imaging provides information mainly related to hepatic steatosis (Keramida *et al* 2014a, 2014b) and does not show a potential for measuring liver inflammation (Wang *et al* 2018), dynamic FDG-PET with improved kinetic modeling has been demonstrated to be promising for non-invasively assessing liver inflammation by quantifying the FDG blood-to-tissue transport rate K_1 (Sarkar *et al* 2017, Wang *et al* 2017, 2018, Sarkar *et al* 2019). Because the liver receives dual blood supplies from the hepatic artery and portal vein (Keiding 2012), accurate liver PET kinetic modeling and quantification of K_1 require the knowledge of dual-blood input function (DBIF) (Brix *et al* 2001, Munk *et al* 2001, Wang *et al* 2018). Although the arterial input function can be derived from the aortic region on dynamic PET images, it can be difficult to extract the portal vein input function from PET images. The limited spatial resolution of PET and small anatomic size

of the portal vein can result in serious partial volume effects and high noise in the image-derived input function (Mourik *et al* 2008).

Traditional single-input kinetic modeling neglects the difference between the hepatic artery input function and portal vein input function, resulting in inaccuracy in kinetic parameter estimation (Brix *et al* 2001, Munk *et al* 2001). Existing population-based DBIF approaches (Brix *et al* 2001, Munk *et al* 2001, Winterdahl *et al* 2011) use the model parameters pre-determined by population means that were commonly derived using arterial blood sampling in animal studies, which however can become ineffective in human studies. Modified models (Kudomi *et al* 2009, Garbarino *et al* 2015) have been proposed but still have certain limitations, for example requiring extraction of multiple different liver time activity curves (TACs) or an additional gut TAC, which may present challenges in clinical applications. In contrast, the optimization-derived DBIF model (Wang *et al* 2018) employs mathematical optimization to jointly estimate the parameters of DBIF and liver FDG kinetics. It directly utilizes image-derived arterial input function, requires no invasive arterial blood sampling or additional ROI operations, and is more adaptive to individual patients. With the improved kinetic modeling, the FDG blood-to-liver transport rate K_1 was statistically associated with histopathologic grades of liver inflammation, while K_1 by the traditional single-blood input function (SBIF) model and population-based DBIF model did not show a statistical significance (Wang *et al* 2018).

Identifiability analysis is crucial for examining the stability of a kinetic model (Gunn 1996, Mankoff *et al* 2006, Delbary *et al* 2016). It characterizes whether or not the unknown parameters of a specified model can be uniquely determined from noise-free data (i.e. structural identifiability (Bellman and Astrom 1970, Anderson 1983)) and how reliably these parameters can be estimated from noisy measurements (i.e. practical identifiability (Miao *et al* 2008, 2011)). Depending on the condition under which the mapping from the parameter space to the input/output space is one-to-one, there is global structural identifiability (one-to-one mapping is valid in the whole parameter space) and there is local structural identifiability (one-to-one mapping is valid locally in the parameter space). Note that even if a parameter is structurally identifiable, it may not be estimated with adequate accuracy from real measurements. Among different methods for identifiability analysis (Miao *et al* 2011), the Laplace transform (Bellman and Astrom 1970) is frequently used for structural identifiability analysis, and computer simulation based on Monte Carlo sampling is the most effective method for analyzing practical identifiability (Miao *et al* 2008).

In dynamic PET, most of the popular kinetic models follow the first-order ordinary differential equations with linear parameters and are commonly structurally identifiable. Hence, previous identifiability studies in dynamic PET focused on practical identifiability analysis (Mankoff *et al* 1998, Muzi *et al* 2005, 2006, El Fakhri *et al* 2009, Doot *et al* 2010). For dual-input kinetic modeling, the optimization-derived DBIF model contains two additional parameters when compared with traditional SBIF and population-based DBIF model. While the new model has improved the practical correlation of FDG K_1 with histology, the increased number of free parameters may potentially increase variance in kinetic parameter estimation, but little is known so far on the quantitative aspects of the modeling.

In this paper, we conduct a theoretical analysis using the Laplace transform to assess the structural identifiability and conduct a computer simulation to evaluate the practical identifiability using patient data of liver inflammation. The results from this study can be used to indicate the quantification accuracy and precision of model parameters and provide guidance for further improving kinetic modeling of dynamic liver PET data.

2. Structural identifiability analysis using the Laplace transform

2.1. Compartmental modeling by differential equations

Most compartmental models in dynamic PET imaging can be described by the following first-order ordinary differential equations:

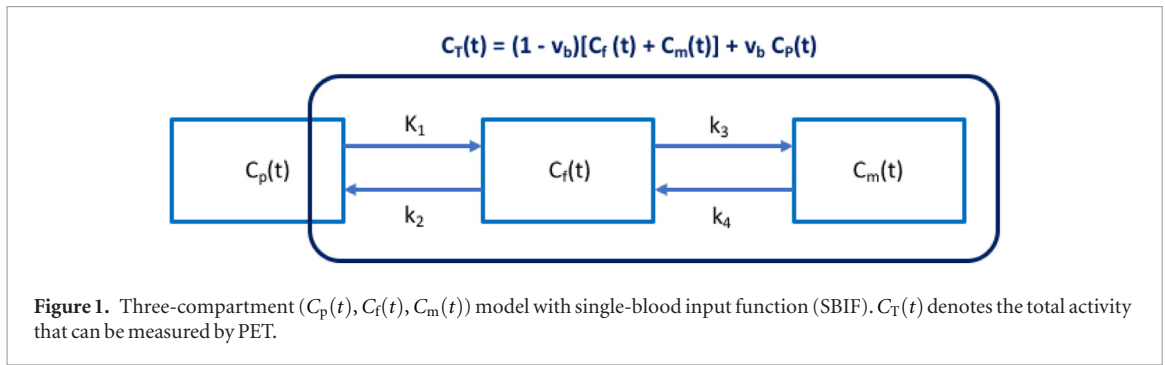
$$\frac{dc(t)}{dt} = \mathbf{A}c(t) + \mathbf{b}u(t), \quad (1)$$

$$C_T(t) = \mathbf{w}^T c(t) + vu(t), \quad (2)$$

$$\mathbf{c}(0) = \mathbf{0}, \quad (3)$$

where t is time; $\mathbf{c}(t) = [c_1(t), c_2(t), \dots, c_n(t)]^T$ is the system states which are assumed to be zero at initial time, where c_i represents the time activity of the i th compartment and n is the number of tissue compartments; $u(t)$ is the system input, often representing the blood input function in dynamic PET; $C_T(t)$ is the system output, i.e. the measured time activity curve (TAC) by PET; \mathbf{A} is a n by n matrix, \mathbf{b} is a n by 1 vector, \mathbf{w} is a n by 1 vector and v is a scalar vector. \mathbf{A} , \mathbf{b} , \mathbf{w} and v are composed of the kinetic parameters $\boldsymbol{\theta} = (\theta_1, \theta_2, \dots, \theta_m)$ to be determined.

For a commonly used 3-compartment model (figure 1) such as for dynamic FDG-PET imaging, we have



$$u(t) = C_p(t), \quad (4)$$

$$\mathbf{c}(t) = [C_f(t), C_m(t)]^T, \quad (5)$$

$$\mathbf{A} = \begin{bmatrix} -(k_2 + k_3) & k_4 \\ k_3 & -k_4 \end{bmatrix}, \quad (6)$$

$$\mathbf{b} = [K_1, 0]^T, \quad (7)$$

$$\mathbf{w} = [1 - v_b, 1 - v_b]^T, \quad (8)$$

$$v = v_b, \quad (9)$$

where $C_p(t)$ is the plasma input function; $C_f(t)$ and $C_m(t)$ are the concentration in the free FDG and metabolized FDG compartments, respectively. The superscript ‘ T ’ denotes matrix or vector transpose. $\boldsymbol{\theta} = [v_b, K_1, k_2, k_3, k_4]^T$ with K_1, k_2, k_3, k_4 denoting the rate constants of FDG transport among compartments. v_b denotes the fractional blood volume.

The optimization-derived DBIF model (Wang *et al* 2018) for analyzing dynamic liver PET data is shown in figure 2 and can be described using the following expressions:

$$u(t) = C_A(t), \quad (10)$$

$$\mathbf{c}(t) = [C_f(t), C_m(t), C_{PV}(t)]^T, \quad (11)$$

$$\mathbf{A} = \begin{bmatrix} -(k_2 + k_3) & k_4 & K_1(1 - f_A) \\ k_3 & -k_4 & 0 \\ 0 & 0 & -k_a \end{bmatrix}, \quad (12)$$

$$\mathbf{b} = [K_1 f_A, 0, k_a]^T, \quad (13)$$

$$\mathbf{w} = [1 - v_b, 1 - v_b, v_b(1 - f_A)]^T, \quad (14)$$

$$v = v_b f_A \quad (15)$$

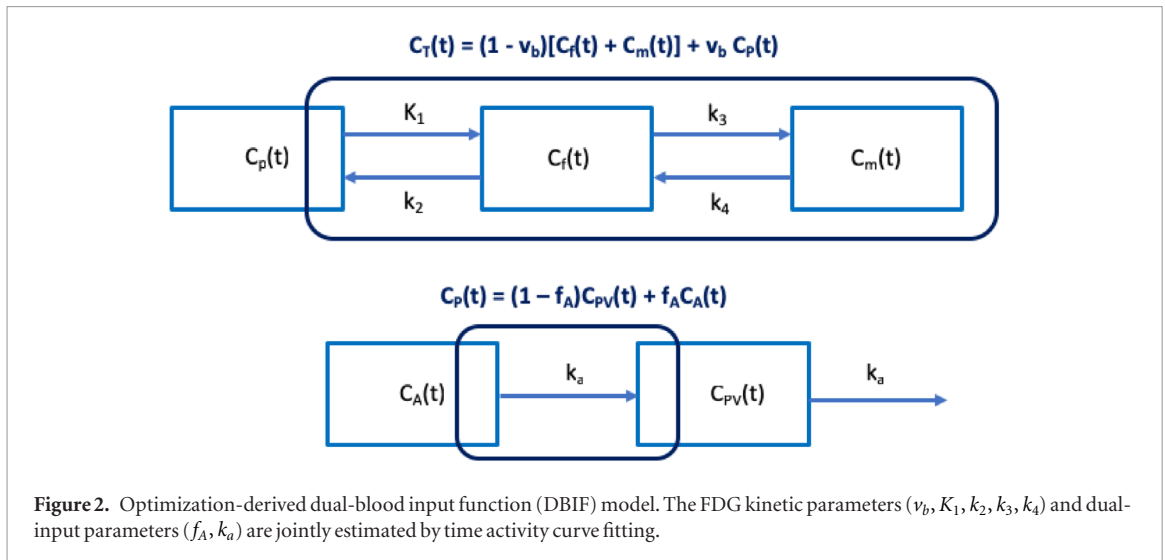
where $C_A(t)$ denotes the blood input function extracted from the hepatic artery; $C_{PV}(t)$ is the portal vein input function; k_a is the rate constant with which FDG flows through the gastrointestinal system. f_A is the fraction of hepatic artery contribution to the overall liver blood flow. The parameters to be determined are $\boldsymbol{\theta} = [v_b, K_1, k_2, k_3, k_4, k_a, f_A]^T$.

2.2. Laplace transform for structural identifiability analysis

The Laplace transform method is a popular method in the field of system theory for analyzing differential equations (Tsien 1954, Oppenheim *et al* 1996). After the transform, the time derivative $\partial/\partial t$ becomes a multiplication of frequency s , thus simplifying the mathematical analysis. Taking the Laplace transform of equations (1) and (2) and making use of equation (3), one has

$$s\tilde{\mathbf{c}}(s) = \mathbf{A}\tilde{\mathbf{c}}(s) + \mathbf{b}\tilde{u}(s), \quad (16)$$

$$\tilde{o}(s) = \mathbf{w}^T \tilde{\mathbf{c}}(s) + v\tilde{u}(s), \quad (17)$$



where

$$\tilde{f}(s) = \int_0^{\infty} f(t)e^{-st} dt \quad (18)$$

represents the Laplace transform of any function f in the time domain.

The system input–output relation can then be expressed as

$$\tilde{o}(s) = \Phi(s)\tilde{u}(s), \quad (19)$$

where $\Phi(s)$ is called the transfer function in the frequency domain,

$$\Phi(s) = [\mathbf{w}^T(s\mathbf{I} - \mathbf{A})^{-1}\mathbf{b}] + v, \quad (20)$$

with \mathbf{I} denoting the identity matrix. $\Phi(s)$ can be further expressed as a fractional function

$$\Phi(s) = \frac{N(s)}{D(s)}, \quad (21)$$

where both the numerator $N(s)$ and denominator $D(s)$ are a polynomial of the frequency s :

$$D(s) \triangleq \sum_{i=0}^r D_i s^i = \sum_{i=0}^r \alpha_i(\boldsymbol{\theta}) s^i, \quad (22)$$

$$N(s) \triangleq \sum_{i=0}^r N_i s^i = \sum_{i=0}^r \beta_i(\boldsymbol{\theta}) s^i, \quad (23)$$

with r being the highest order of the polynomials of s . N_i is the coefficient of order i in $N(s)$ and D_i is the coefficient of order i in $D(s)$. $\alpha_i(\boldsymbol{\theta})$ and $\beta_i(\boldsymbol{\theta})$ describe the theoretical model of N_i and D_i with respect to $\boldsymbol{\theta}$, respectively.

The structural identifiability analysis examines if the unknown parameter set $\boldsymbol{\theta}$ can be uniquely determined from $\{N_i, D_i\}_{i=0}^r$ following the equation set:

$$\alpha_i(\boldsymbol{\theta}) = D_i, \quad (24)$$

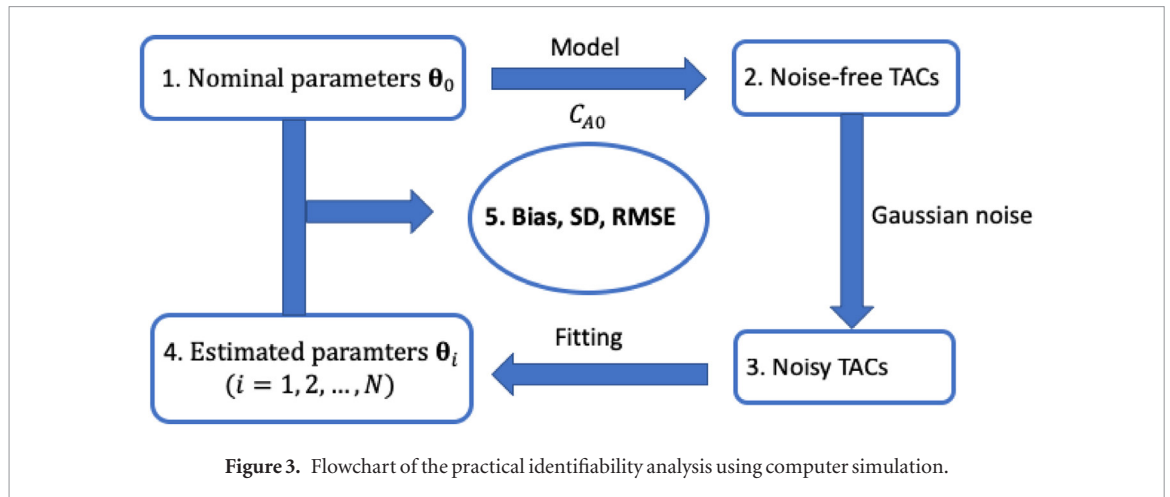
$$\beta_i(\boldsymbol{\theta}) = N_i, \quad (25)$$

for i from 0 to r . If there are arbitrary solutions for the equations, the model structure is non-identifiable. If the equations have a unique solution for any admissible input and in the whole parameter space, the model structure is called globally identifiable. If the solution only holds unique for a neighborhood of some points $\boldsymbol{\theta}_*$ in the parameter space, the structure is then locally identifiable. The single-input compartmental model for dynamic FDG-PET is globally identifiable (Gunn 1996). A brief proof is provided in the appendix for the reader convenience.

2.3. Structural identifiability of dual-input kinetic modeling

For the optimization-derived DBIF model, based on the derivations detailed in the appendix, we can derive

$$k_a^3 - D_2 k_a^2 + D_1 k_a - D_0 = 0, \quad (26)$$



which is a cubic equation of k_a . In the real parameter space, the number of roots for k_a is at least 1 and at most 3.

Similarly, for f_A we have,

$$N_0 f_A^3 - (N_1 k_a) \cdot f_A^2 + (N_2 k_a^2) \cdot f_A - N_3 k_a^3 = 0, \quad (27)$$

which is also a cubic equation when k_a is fixed. The number of roots for f_A with given k_a in the non-negative parameter space is at least 1 and at most 3.

These results indicate that k_a and f_A are not globally identifiable because they may have multiple solutions.

However, given there is at least one nonnegative root for k_a and f_A , they are locally identifiable. In practice, this requires a proper definition of initial estimates, lower and upper bounds for the parameters. Once k_a and f_A are determined, K_1, k_2, k_3, k_4 can then be determined respectively.

3. Practical identifiability analysis using computer simulation

3.1. Computer simulation

3.1.1. Overall description

The process of the computer simulation is described in figure 3. For each simulation, the nominal kinetic parameters θ_0 and the input function $C_A(t)$ were extracted from one of the human patient datasets and used to generate the noise-free liver tissue time activity curves (TAC). Independently and identically distributed noise was then added to the noise-free TAC using random sampling, following a defined time-varying Gaussian noise model to generate $N = 1000$ realizations of noisy tissue TAC. We then fit the noisy liver tissue TACs and estimate the kinetic parameters of the optimization-derived DBIF kinetic model using nonlinear least-square fitting with the Levenberg–Marquardt algorithm described in our previous work (Wang et al 2018). Normalized bias, standard deviation (SD) and root mean square error (RMSE) were calculated to assess the statistical properties of each kinetic parameter estimation. This same simulation was done for multiple patient data sets.

In addition to the kinetic parameters directly estimated by the model, the FDG net influx rate $K_i = K_1 k_3 / (k_2 + k_3)$ was also evaluated.

3.1.2. Human liver FDG kinetics and histological data

Fourteen patients with NAFLD were included in this study to provide nominal kinetic parameters (Wang et al 2018). These patients had a liver biopsy as a part of routine clinical care or for enrollment in clinical trials. Liver biopsies were scored according to the nonalcoholic steatohepatitis clinical research network (NASH-CRN) criteria. An overall liver inflammation score (range 0–5) is obtained by combining the scores of lobular inflammation and ballooning degeneration (hepatocyte injury) as both reflect the inflammatory status in the total NAFLD activity (Sarkar et al 2019). Dynamic PET studies were performed using the GE Discovery 690 PET/CT scanner (axial field-of-view: 16 cm) at the UC Davis Medical Center. Each patient was injected with 10 mCi ^{18}F -FDG. One-hour dynamic PET scanning was performed for a single bed position with the liver centered in the scanner field-of-view. A transmission CT scan was performed at the end of PET scan for attenuation correction. Dynamic PET data were reconstructed into 49 time frames (30×10 s, 10×60 s, and 9×300 s) using the vendor software with the standard ordered subsets expectation maximization algorithm with 2 iterations and 32 subsets.

Eight spherical regions of interest (ROI), each with 25 mm in diameter, were placed on eight segments of the liver excluding the caudate lobe and avoiding any major blood vessels. An illustration is shown in figure 4. A TAC was extracted from each liver-segment ROI. The average of these TACs was used to represent the tissue TAC in the whole-liver region. An additional volumetric ROI was placed in the descending aorta region to extract

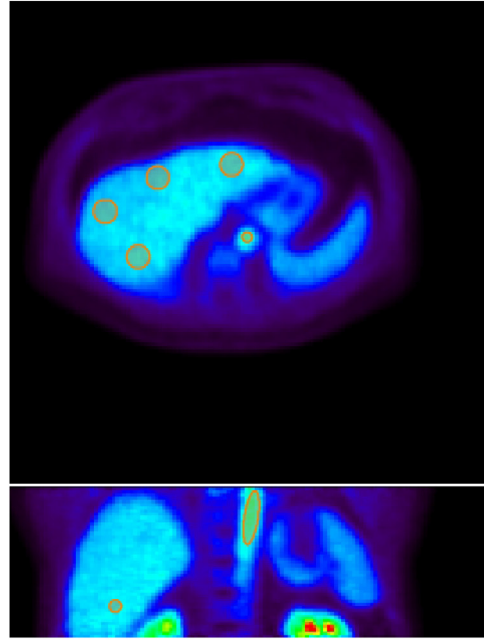


Figure 4. Illustration of volumetric ROIs in the liver segments and aorta in 2D planes. Top: a transverse plane showing the aortic ROI and four of eight spherical liver ROIs; Bottom: a coronal plane showing the aortic ROI and one of eight spherical liver ROIs. ROIs are overlaid on the PET image of one-hour duration. All the spherical liver ROIs are of 25 mm in diameter.

image-derived aortic input function. The optimization-derived DBIF model was used to derive the regional liver FDG kinetics at both the whole-liver ROI level and liver-segment ROI level. Hence there are a total 14 whole-liver FDG kinetic parameter sets and 112 liver-segment kinetic parameter sets from the 14 patient scans.

3.1.3. Noise model of TACs

The reconstructed time activity in the frame m , c_m , can be approximately modeled by an i.i.d. Gaussian distribution (Carson *et al* 1993, Wu and Carson 2002),

$$c_m \sim \text{Gaussian}(\bar{c}_m, S_c \cdot \delta_m) \quad (28)$$

where $\{\bar{c}_m\}$ denotes the noise-free TAC and S_c is a scaling factor adjusting the amplitude of the unscaled standard deviation (SD) δ_m ,

$$\delta_m = \sqrt{\frac{\bar{c}_m \exp(\lambda t_m)}{\Delta t_m}}, \quad (29)$$

where t_m is the mid-time of frame m , Δt_m is the scan duration of the time frame m , and $\lambda = \ln 2/T_{1/2}$ is the decay constant of radiotracer with $T_{1/2}$ (min) being the half-life. For ^{18}F -FDG, $T_{1/2} = 109.8$ min.

Equivalently, the normalized residual difference follows a zero-mean Gaussian with the SD S_c :

$$\Delta c_m \triangleq \frac{c_m - \bar{c}_m}{\delta_m} \sim \text{Gaussian}(0, S_c). \quad (30)$$

From our patient study, we have a total 14 patients \times 49 frames/patient = 686 samples for Δc_m extracted at the whole-liver ROI level. The scale S_c can then be determined by approximating the histogram of Δc_m using the Gaussian with the standard deviation S_c . Similarly, we have a total 686 \times 8 = 5488 samples to estimate S_c for the noise level at the liver-segment ROI level. Note that equation (30) is only used for deriving the global scaling factor of the noise level, not indicating the noise is uniform across frames. The actual noise of dynamic time frames, as modeled by equation (28), is time-varying and depends on the activity and scan duration of each frame.

3.2. Analysis methods

3.2.1. Sensitivity analysis

The sensitivity of a model TAC $C_T(t)$ with regard to a kinetic parameter θ_k is defined by

$$S_{\theta_k}(t) = \frac{\partial C_T(t)}{\partial \theta_k} \quad (31)$$

and the normalized sensitivity is defined as

$$\hat{S}_{\theta_k}(t) = S_{\theta_k}(t) \cdot \frac{\theta_k}{C_T(t)} \quad (32)$$

where k denotes the k th element of the kinetic parameter set θ and $\partial C_T(t)/\partial \theta_k$ denotes the partial derivative of $C_T(t)$ with respect to θ_k (Mankoff *et al* 2006).

The sensitivity function $S_{\theta_k}(t)$ illustrates how much the model TAC would change over time in response to a small change in the individual parameter θ_k . The larger the absolute value of the sensitivity is, the more sensitive the TAC would be to the change in the chosen parameter. While $S_{\theta_k}(t)$ is used to evaluate the sensitivity over time for a specified parameter θ_k , the normalized sensitivity function $\hat{S}_{\theta_k}(t)$ is more appropriate to compare the sensitivities across different parameters.

To evaluate the interference between different kinetic parameters, a correlation matrix \mathbf{M} is defined using the sensitivity functions (Miao *et al* 2011):

$$M_{ij} = \text{corr}(S_{\theta_i}, S_{\theta_j}) \quad (33)$$

and can be equivalently calculated using the Pearson's correlation coefficient 'corr'. M_{ij} denotes the interaction between θ_i and θ_j in producing a change in the model TAC. Values close to ± 1 indicate the parameters cannot be estimated independently.

We evaluated the sensitivity functions and correlation matrix based on the mean of the kinetic parameters of the 14 patient datasets.

3.2.2. Quality of parameter estimation

For each true kinetic parameter θ_k^0 , the normalized bias, SD and RMSE of the kinetic parameter estimate $\hat{\theta}$ are calculated as

$$\text{Bias}(\hat{\theta}_k) = \frac{\text{Mean}(\hat{\theta}_k) - \theta_k^0}{\theta_k^0} \times 100\% \quad (34)$$

$$\text{SD}(\hat{\theta}_k) = \frac{1}{\theta_k^0} \sqrt{\frac{1}{N-1} \sum_{n=1}^N [\hat{\theta}_k - \text{Mean}(\hat{\theta}_k)]^2} \times 100\% \quad (35)$$

$$\text{RMSE}(\hat{\theta}_k) = \sqrt{\frac{1}{N} \sum_{n=1}^N \left(\frac{\hat{\theta}_k - \theta_k^0}{\theta_k^0} \right)^2} \times 100\% \quad (36)$$

where $\text{Mean}(\cdot)$ represents the mean of the kinetic parameter estimates $\hat{\theta}_k$, respectively.

3.2.3. Comparison of different fitting options

The initial values of the kinetic parameter set $[v_b, K_1, k_2, k_3, k_4, k_a, f_A]$ were set to $[0.01, 1.0, 1.0, 0.01, 0.01, 1, 0.01]$ with lower bound $[0, 0, 0, 0, 0, 1, 0]$ and upper bound $[1, 10, 10, 1, 0.1, 10, 1]$. The weighting factor for the fitting was also initially set to be uniform as used in our previous study (Wang *et al* 2018). Nevertheless, our initial analysis indicates that this initialization may result in significant bias in K_1 for some patient datasets. To solve this problem, we proposed two modifications to improve the fitting and K_1 quantification. Instead of using a single initial value 1.0, we repeated the TAC fitting using different K_1 initial values (0.5, 1.0, 1.5, 2.0, 2.5, 3.0). The one with minimum least-squares of TAC fitting was used as the optimal. This modification can reduce the effect of getting stuck at a local solution of K_1 . In addition, we also tested a nonuniform weighting scheme $w_m = \Delta t_m \cdot \exp(-\lambda \cdot t_m)$ versus the uniform weighting scheme $w_m = 1$. As K_1 is the major parameter of interest, these different approaches were compared for reducing the bias of K_1 .

3.2.4. Comparison with simplified kinetic models

Based on our previous results (Wang *et al* 2018), the optimization-derived DBIF model can fit the patient data well. However, it is a more complex model involving additional free parameters. An open question is whether a simplified model can provide a similar performance of quantification as the complex model, assuming the DBIF model is physiologically correct.

Here we evaluated two simplified models: (1) traditional SBIF model, which corresponds to the optimization-derived DBIF model with $f_A = 1$ and $k_a = 0$; (2) population-based DBIF model (see Wang *et al* (2018) for detail). In addition, we found in our previous work (Wang *et al* 2018) that the optimization-derived DBIF model with free k_4 can better fit the patient data than neglecting k_4 (i.e. $k_4 = 0$) during the fitting. So we also further evaluated the differences between these two options. We evaluated the bias, SD and RMSE of the kinetic parameter estimation for each model.

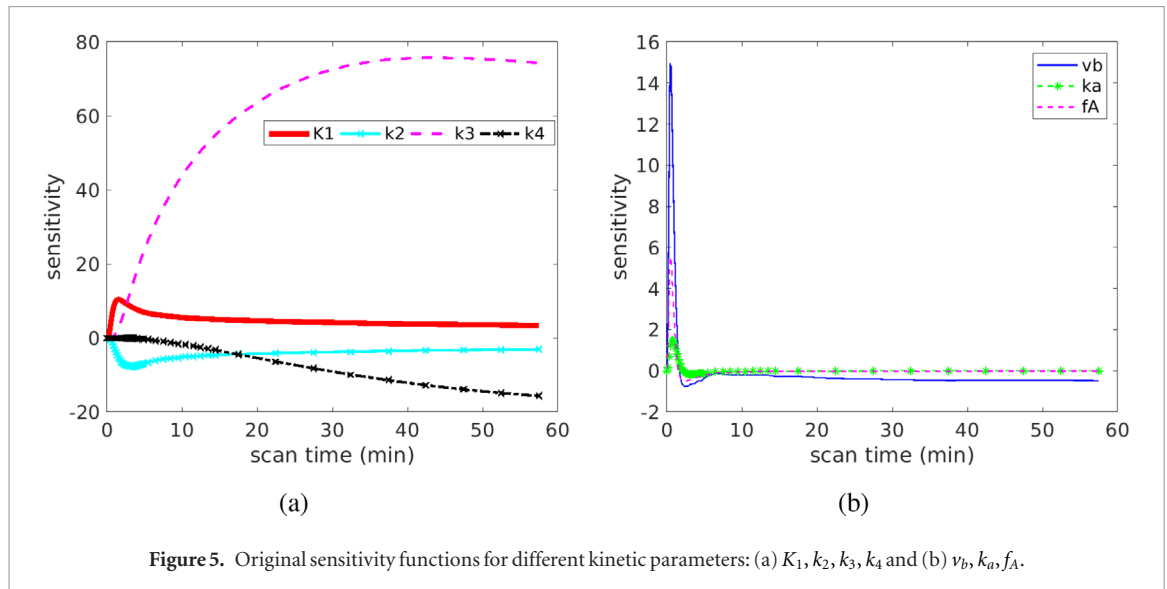


Figure 5. Original sensitivity functions for different kinetic parameters: (a) K_1 , k_2 , k_3 , k_4 and (b) v_b , k_a , f_A .

3.2.5. Parameter estimation accuracy over clinical range

In addition to evaluating the bias and SD for each individual kinetic data set, we also evaluated the overall performance of the model over a wide parameter range following the approach used in Mankoff *et al* (1998). We conducted a Pearson's linear correlation analysis to assess the closeness between θ_k^0 and $\hat{\theta}_k$ of all patients. The closer the correlation coefficient r is to 1, the more reliable the parameter can be estimated by the model over a wide range. In this study, we used the liver-segment kinetic parameter sets to allow a wide range of values to form the correlation plot.

3.2.6. Variation of the correlation between FDG K_1 and liver inflammation

Our previous study of a patient cohort of 14 patients had demonstrated that the FDG K_1 parameter correlated with histological liver inflammation score with a statistical significance. Here we evaluated the reliability and uncertainty associated with the correlation between PET K_1 and histology. This was done by repeating the estimation of 14 patient kinetic parameter sets at the whole-liver ROI level for $N = 1000$ noisy realizations using the computer simulation study (figure 3). The Pearson's correlation r between liver inflammation score and K_1 was calculated for each realization. The bias, standard deviation and 95% confidence interval of r were then calculated to assess the reliability.

3.3. Results

3.3.1. Sensitivity analysis

Figure 5 shows the plots of original sensitivity functions for different kinetic parameters in the optimization-derived DBIF model. The parameter set was the population means $\bar{\theta} = [0.0185, 1.0013, 1.1400, 0.0149, 0.0586, 1.9849, 0.0405]^T$. Overall, the sensitivities of the TAC to K_1 and k_2 reached their extreme values (peak or dip) at early times and became decayed at late times. In contrast, the sensitivities of the TAC to k_3 and k_4 had larger magnitudes at late times than early times. This suggests the early-time data may contribute more to the estimation of K_1 and k_2 and late-time data dominate more the estimation of k_3 and k_4 . The TAC was also sensitive to the vascular-related kinetic parameters v_b , k_a , f_A mainly at early time.

Figure 6 shows the normalized sensitivity functions, which allow a better comparison across different kinetic parameters. In the first 60 minutes, the TAC is more sensitive to K_1 and k_2 than to k_3 and k_4 . The correlation between the normalized sensitivity functions is summarized in table 1. The curves of K_1 and k_2 have opposite signs. Their shapes are similar at late times but are different at early times, resulting in a modest correlation with each other ($r = -0.67$). A similar effect also holds true between k_3 and k_4 ($r = -0.87$). The curve of v_b is almost fully overlapped with that of f_A , indicating the correlation is high and it is difficult to differentiate them from each other. Because the curve shape of v_b or f_A is different from the shape of K_1 , the coupled effect of v_b and f_A should have a minimal effect on the estimation of K_1 , as indicated by the small correlation.

3.3.2. Determination of the noise model parameter

Figure 7 shows the histograms of the normalized residual error Δc_m at the whole-liver ROI level and the liver-segment ROI level. Note that all 49 frames with various scan durations (10 s, 60 s, 300 s) of each patient scan are included for this analysis. The obtained S_c values are 0.3 and 0.6, respectively. The distribution of Δc_m approximately follows a Gaussian in both cases. We therefore used these two S_c values to define the noise standard

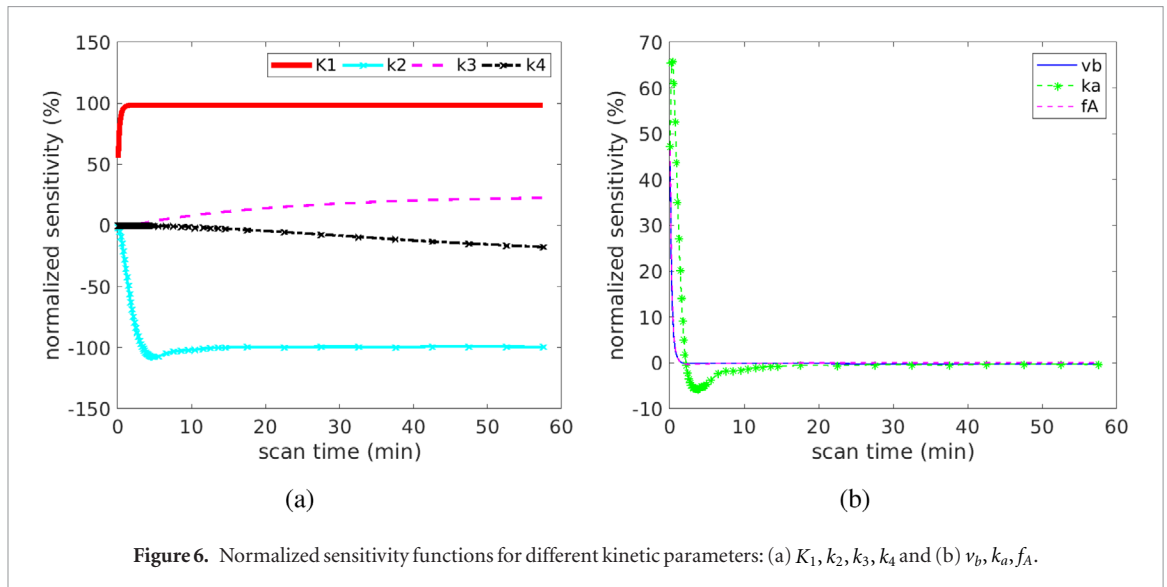


Figure 6. Normalized sensitivity functions for different kinetic parameters: (a) K_1 , k_2 , k_3 , k_4 and (b) v_b , k_a , f_A .

Table 1. Correlation matrix of the sensitivity functions.

	K_1	k_3	k_4	k_2	v_b	k_a	f_A
K_1	1.00	-0.56	0.54	-0.67	-0.18	0.16	-0.27
k_3		1.00	-0.87	0.14	-0.39	-0.40	-0.31
k_4			1.00	-0.33	0.21	0.18	0.13
k_2				1.00	0.68	0.59	0.73
v_b					1.00	0.79	1.00
k_a						1.00	0.77
f_A							1.00

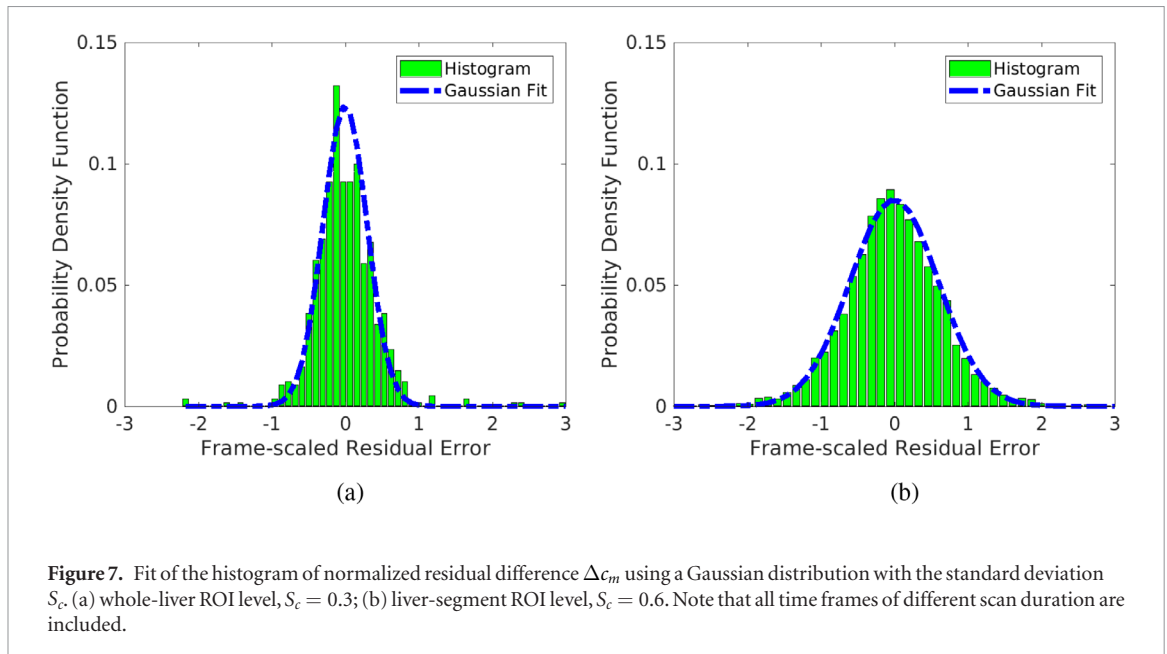
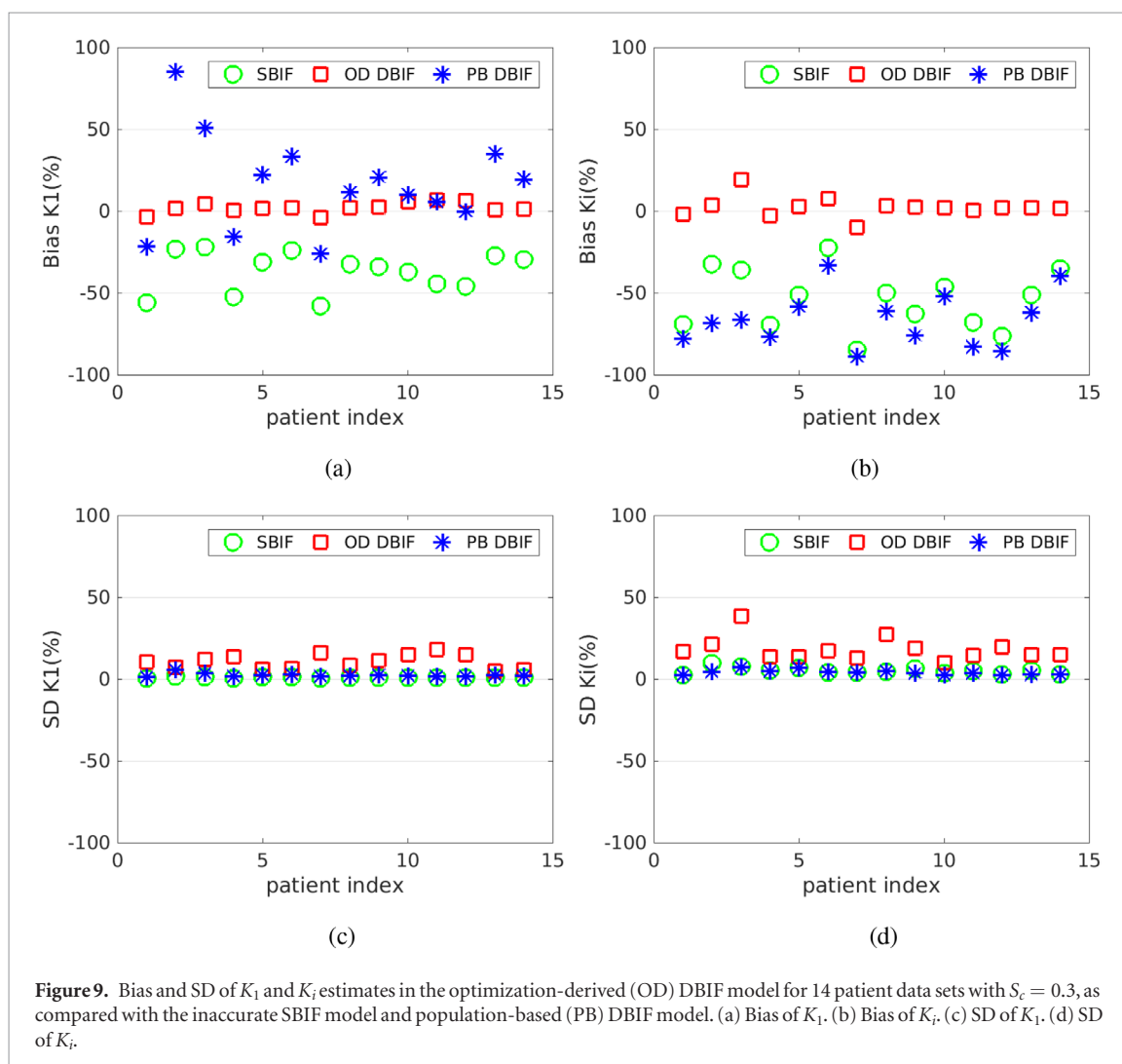
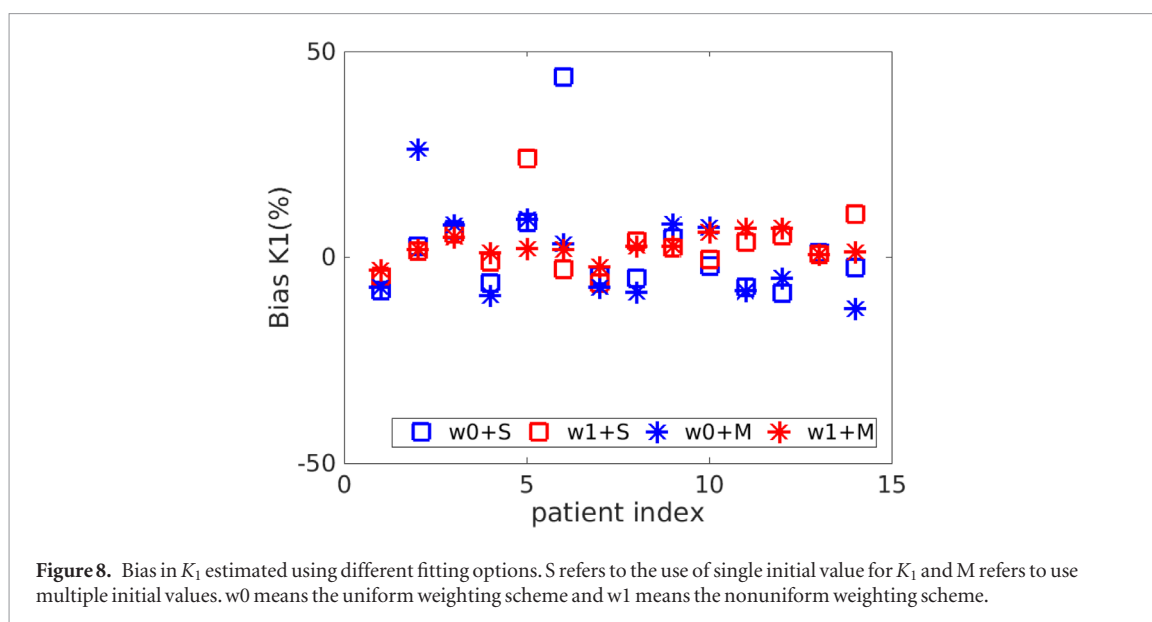


Figure 7. Fit of the histogram of normalized residual difference $\Delta\epsilon_m$ using a Gaussian distribution with the standard deviation S_c . (a) whole-liver ROI level, $S_c = 0.3$; (b) liver-segment ROI level, $S_c = 0.6$. Note that all time frames of different scan duration are included.

deviation for the whole-liver ROI level and liver-segment level in the simulation studies. Note that the size of whole-liver ROI is 8 times that of the liver-segment ROI, which ideally should reduce the noise standard deviation by a factor of $\sqrt{8} \approx 2.8$. However, pixels in the liver ROI are not fully independent of each other and therefore the reduction in S_c may be smaller than that suggested by the ROI size increase.

3.3.3. Comparison of different fitting options

Figure 8 shows the comparison of different initialization and weighting schemes for each patient at the whole-liver ROI level ($S_c = 0.3$). The K_1 single-initialization strategy resulted in bias in K_1 in several patient datasets. The bias can be reduced when the multi-initialization strategy was used, which however did not provide a universal



improvement over all patients. On the other hand, use of nonuniform weighting for TAC fitting led to reduced bias in some patients. The benefit of these two modifications were maximized when they were used together and the bias in K_1 remained small in all patients. Thus, the multi-initialization for K_1 and nonuniform weighting scheme were used in this work for all subsequent analysis.

Table 2. Absolute bias and SD of liver FDG kinetic parameter estimates by different kinetic models. The absolute bias and SD are averaged over 14 patient data sets.

	OD DBIF		SBIF		PB DBIF	
	Bias (%)	SD (%)	Bias (%)	SD (%)	Bias (%)	SD (%)
K_1	3.2	10.8	36.7	1.1	25.5	2.6
k_2	3.5	11.6	40.1	1.1	21.7	2.4
k_3	5.0	19.7	56.1	5.2	69.4	4.0
k_4	8.1	44.0	85.1	9.4	90.7	8.5
K_i	4.5	18.3	53.8	5.2	66.1	4.2

Table 3. RMSE (%) of liver FDG kinetic parameter estimates by different kinetic models. The RMSE is averaged over 14 patient data sets.

	OD DBIF	SBIF	PB DBIF
	RMSE (%)	RMSE (%)	RMSE (%)
K_1	11.3	36.7	25.8
k_2	12.1	40.1	21.9
k_3	20.6	56.5	69.6
k_4	45.2	86.1	91.8
K_i	19.1	54.1	66.3

3.3.4. Bias of simplified kinetic models

Figure 9 show the bias and SD of K_1 and K_i estimated by three different kinetic models at the noise level of $S_c = 0.3$. When the traditional SBIF model was used for fitting the TAC, K_1 was underestimated with an average 37% bias. K_1 by the population-based DBIF was also underestimated by 26%. In comparison, the mean absolute bias of K_1 by the optimization-derived DBIF model was only about 3% and the biases of individual patients all remain small. For the estimation of K_i , the SBIF and population-based DBIF resulted in an underestimation of approximately 60%, as compared with an average bias of less than 5% by the optimization-derived DBIF model.

The bias reduction achieved by the optimization-derived DBIF model came with the price of increased SD, as shown in figures 9(c) and (d). The average SD was 11% for K_1 and 18% for K_i by the optimization-derived DBIF, as compared to less than 6% by the other two models. This can be explained by the increased number of free parameters in the optimization-derived DBIF model.

The results of the averaged absolute bias and SD across different patients are summarized in table 2 for all FDG transport rate parameters. Generally, with the assumption of the TACs following the DBIF model, the simplified SBIF model resulted in greater than 35%–85% bias and the population-based DBIF model led to greater than 20%–90% bias in all kinetic estimates. The more accurate optimization-derived DBIF model still had a bias of about 3%–8% in all the kinetic estimates, which can be explained by the highly nonlinear noise propagation and by the structural identifiability of the model being local as opposed to global.

Note that as compared to the simplified SBIF and population-based DBIF models, the increase of SD by the optimization-derived DBIF model was generally smaller than the corresponding bias reduction. This indicates the overall gain of the new model is greater than its loss, as reflected by the RMSE evaluation in table 3. This has led to the improvement in correlating FDG K_1 with histology as we observed in the previous patient study (Wang *et al* 2018).

3.3.5. Effect of neglecting k_4

Figure 10 compares the bias and RMSE of K_1 and K_i between the two fitting options with free k_4 or fixed $k_4 = 0$ for the optimization-derived DBIF model. The averaged bias of K_1 over 14 patient data sets was 3.2% versus 11.9% and the averaged bias of K_i was 4.5% and 48.8% for the two options. While with lower SD, the approach with $k_4 = 0$ generally resulted in higher RMSE especially in K_i estimates than the approach with free k_4 .

3.3.6. Effect of noise levels on kinetic quantification

Table 4 shows the average absolute bias and SD of kinetic parameters estimated by the optimization-derived DBIF model under three noise levels: noise-free ($S_c = 0.0$), noise at the whole-liver ROI level ($S_c = 0.3$), and noise at the liver-segment ROI level ($S_c = 0.6$). While other kinetic parameters had a small bias, the bias of v_b and f_A were surprisingly large even at the noise-free case ($S_c = 0.0$). This can be explained by the fact that the model is locally identifiable with potential multiple solutions. The result is also consistent with the observation on the indifferentiable sensitivity curves of v_b and f_A in figure 5. Despite the large bias in v_b and f_A , the bias of K_1 remained small ($<8\%$). The SD of K_1 increased from 7% to 18% when the noise level was changed from the

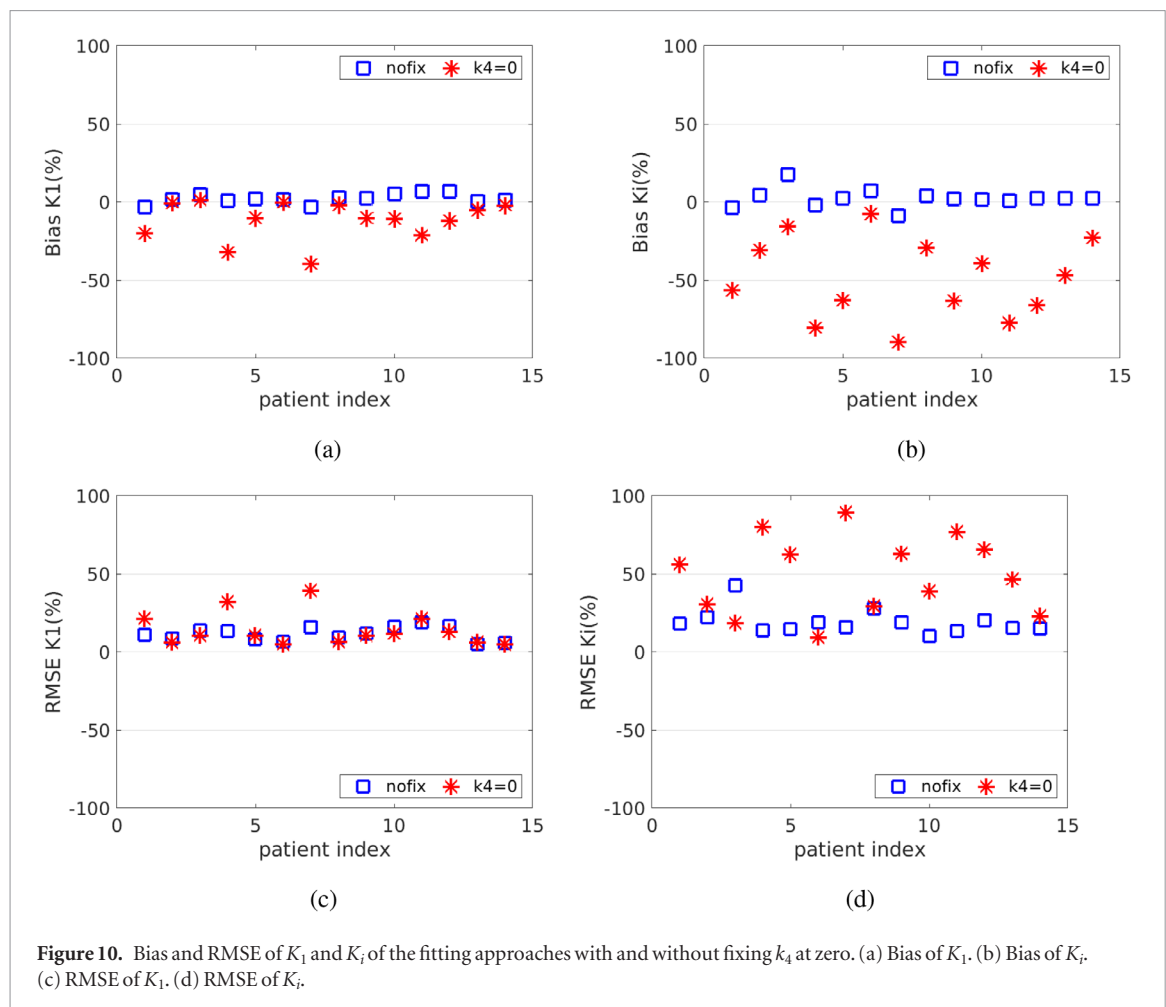


Figure 10. Bias and RMSE of K_1 and K_i of the fitting approaches with and without fixing k_4 at zero. (a) Bias of K_1 . (b) Bias of K_i . (c) RMSE of K_1 . (d) RMSE of K_i .

Table 4. Bias and SD of the kinetic parameters in the optimization-derived DBIF model under three different noise levels: $S_c = 0$ (noise-free), $S_c = 0.3$ (whole-liver ROI level), and $S_c = 0.6$ (liver-segment ROI level).

	$S_c = 0$		$S_c = 0.3$		$S_c = 0.6$	
	Bias (%)	SD (%)	Bias (%)	SD (%)	Bias (%)	SD (%)
K_1	0.6	0	3.2	10.8	7.4	18.3
k_2	0.6	0	3.5	11.6	8.2	19.6
k_3	0.2	0	5.0	19.7	12.4	40.3
k_4	0.1	0	8.1	44.0	22.7	81.6
K_i	0.2	0	4.5	18.3	11.1	37.0
v_b	16.2	0	71.8	206.5	182.6	484.6
k_a	0.6	0	3.9	16.2	6.1	27.6
f_A	16.9	0	38.3	121.9	41.6	142.5

whole-liver ROI level to liver-segment ROI level. The estimation of K_i is more sensitive to noise, with the SD being 18% for the whole-liver ROI level and 37% for the liver-segment ROI level. k_2 had similar accuracy and precision as K_1 and k_3 had similar accuracy and precision as K_i . k_4 had a much higher bias and SD because the scan time (1 h in our study) is not sufficient enough for robust estimation of k_4 , which can be justified from its sensitivity curve.

3.3.7. Parameter estimation accuracy over clinical range

Figure 11 shows the plots of linear correlation between the true values and noisy estimates of different kinetic parameters at the whole-liver ROI noise level. The correlation coefficients under different noise levels for all kinetic parameters are summarized in table 5. As the noise level increased, the correlation coefficients reduced. Both K_1 and K_i were well repeatable against noise. While all other kinetic parameters including (k_2 , k_3 , k_4 , k_a) can be repeated well, the two vascular parameters v_b and f_A are less repeatable.

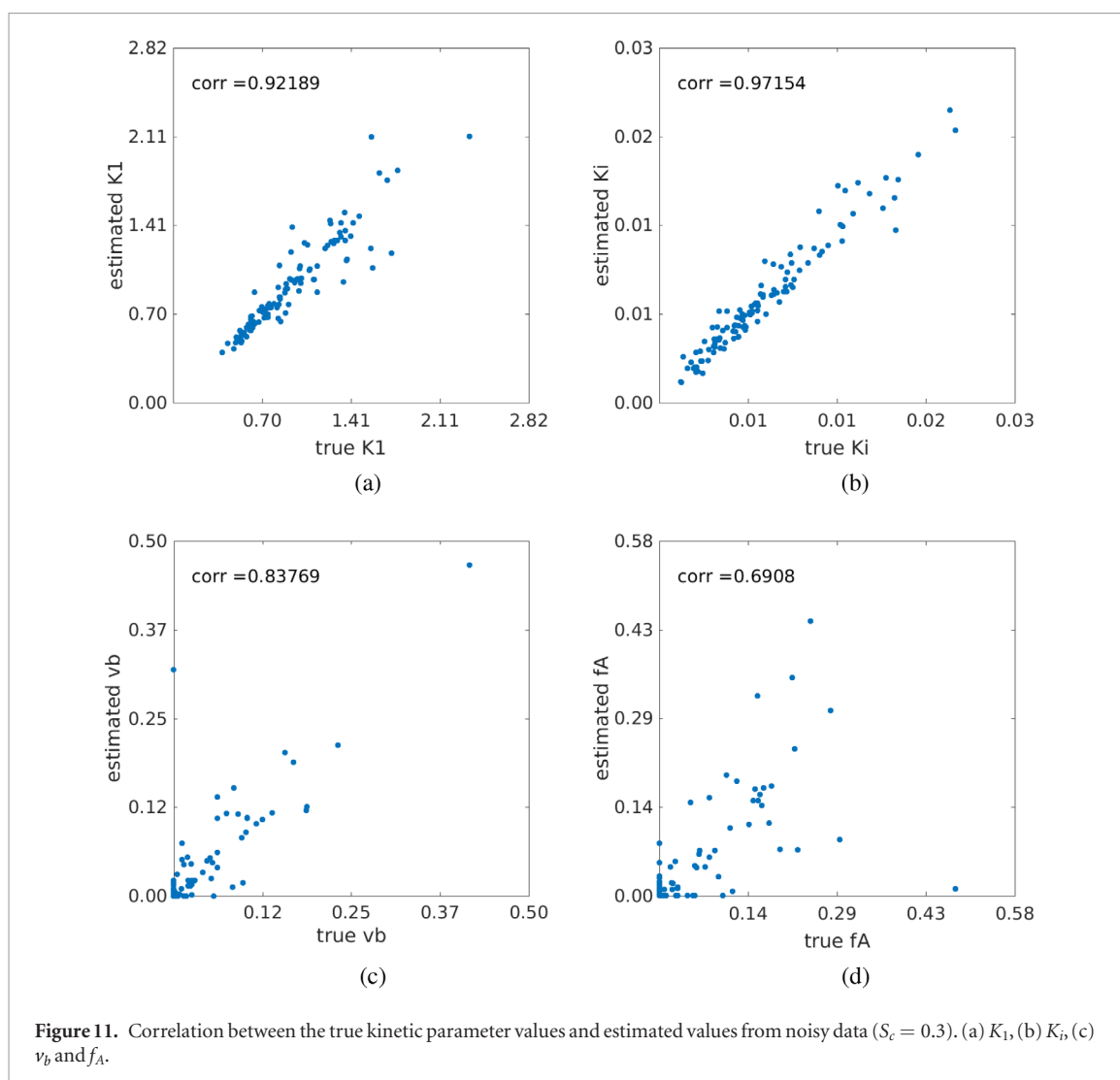
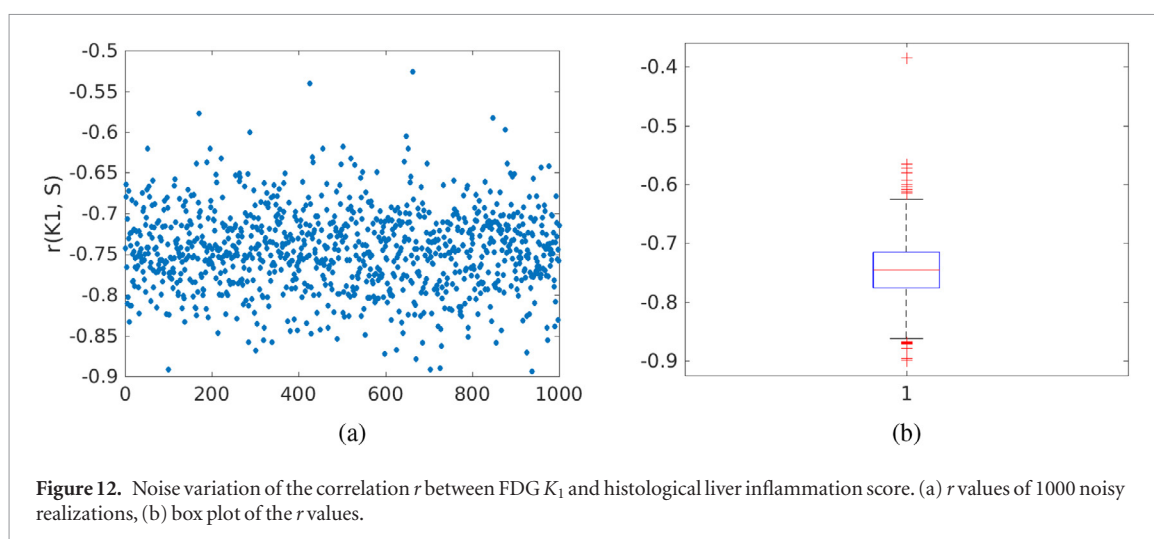


Table 5. Coefficients of the linear correlation between estimated kinetic parameters and their true values.

	v_b	K_1	k_2	k_3	k_4	k_a	f_A	K_i
$S_c = 0.3$	0.84	0.92	0.90	0.97	0.98	0.91	0.69	0.97
$S_c = 0.6$	0.78	0.88	0.83	0.90	0.91	0.79	0.66	0.90



3.3.8. Noise variation of the K_1 correlation with liver inflammation

Figure 12 shows the results of correlating the histological inflammation scores with the FDG K_1 estimates derived from 1000 noisy realizations ($S_c = 0.3$). This investigation quantitates the uncertainty (due to PET measurement noise) associated with the correlation estimation. The Pearson's correlation r between the original K_1 values and liver inflammation scores in the cohort of 14 patients was $r = -0.7618$ ($p = 0.0012$). The 95% confidence interval of the noisy r estimates was estimated to be $[-0.8434, -0.6494]$ with the mean -0.7452 and standard derivation 0.0493 . The percent bias in r was -2.2% and the SD was 6.5% , both approximately close to that in K_1 . The results indicate the noise stability of the estimation of the correlation between FDG K_1 and liver inflammation.

4. Discussion

FDG K_1 by the optimization-derived DBIF model can be a promising PET biomarker for evaluating human liver inflammation in fatty liver disease (Sarkar *et al* 2017, Wang *et al* 2017, 2018, Sarkar *et al* 2019). A more detailed explanation of the possible physiological hypothesis is provided in our previous work (Sarkar *et al* 2019). The focus of the current work is to characterize the identifiability of the optimization-derived DBIF model structure and evaluate the accuracy and precision of K_1 and other kinetic parameters in dynamic liver FDG-PET.

We first conducted a theoretical analysis of the structural identifiability of standard three-compartmental model and the new DBIF model using the Laplacian transform. While standard three-compartmental model is globally identifiable, the new model is locally identifiable due to potential multiple solutions. This suggests that particular care should be given to set the initial values as well as the upper and lower bounds such that the kinetic parameter estimation can properly constrain the optimization problem of TAC fitting with the new model.

We then conducted computer simulations to examine the practical identifiability of the model parameters based on 14 patient datasets which include both dynamic FDG-PET data and histopathology data of human liver inflammation. While the estimation of some kinetic parameters (e.g. f_A and v_b) is associated with large bias and standard deviation, FDG K_1 , the parameter of major interest, has low bias ($\approx 3\%$) and standard deviation ($\approx 11\%$) at the whole-liver ROI level. As demonstrated in the simulation study, fitting liver TACs using the simplified SBIF model or population-based DBIF model may result in significant bias ($>20\%$) in liver K_1 quantification. These results explain why the K_1 by the new model achieved a statistically significant association with liver inflammation in the patient study, while the other two models did not demonstrate success (Wang *et al* 2018).

We also examined the reliability of the new model for liver K_1 quantification over a wide range of values from 0.5 to 2.5 (figure 11). The true K_1 values and their estimates are highly correlated ($r > 0.9$). The stability of K_1 estimation against noise is also preserved in its correlation with liver inflammation (figure 12).

We further studied the effect of nonzero k_4 . Recent interests in whole-body parametric imaging have been growing with the implementation of multi-bed dynamic PET imaging for commercial scanners (Karakatsanis *et al* 2013a, Hu *et al* 2017) and the advent of total-body PET scanners (Cherry *et al* 2017, Badawi *et al* 2019). For parametric imaging of FDG K_1 , k_4 is usually neglected by standard whole-body Patlak parametric imaging (Karakatsanis *et al* 2013a, 2013b). Our computer simulation study suggests that k_4 should not be neglected in the liver if one-hour scan is used, which is consistent with past dynamic FDG studies (Messa *et al* 1992, Okazumi *et al* 1992, Miyazawa *et al* 1993, Karakatsanis *et al* 2014). Full three-compartmental modeling or the generalized Patlak method (Karakatsanis *et al* 2015) can be thereby used to take into account the effect of nonzero k_4 when the liver is involved in the field of view.

A disadvantage of the optimization-derived DBIF model is the increased standard deviation in kinetic parameter estimation, which is basically caused by the increased number of free parameters. To control the standard deviation of K_1 and other parameters of interest, one potential strategy is to add additional constraints in the optimization problem. For example, table 6 compares the bias and standard deviation of kinetic parameters for either estimating or fixing the input function parameter k_a in the optimization of TAC fitting. If k_a is fixed at its true values, the bias and standard deviation of K_1 (and other kinetic parameters) can be largely reduced. This is not surprising because a fixed k_a corresponds to a known portal vein input function. However, the result reported here indicates the potential improvement space if a modified method can be developed to incorporate the prior information of the portal vein input function.

The study also indicates that kinetic quantification at the liver-segment ROI noise level ($S_c = 0.6$) is less reliable than at the whole-liver ROI noise level ($S_c = 0.3$). Both bias and SD become nearly doubled, as shown in table 4. It is worth noting that all the studies were conducted using standard clinical PET. The high-sensitivity EXPLORER scanner can increase sensitivity of PET by a factor of 4–5 for imaging a single organ (Poon *et al* 2012, Zhang *et al* 2017, Cherry *et al* 2018, Badawi *et al* 2019), which can reduce the liver-segment ROI noise level from current $S_c = 0.6$ to $S_c = 0.3$, i.e. by a factor equal to the square-root of the sensitivity improvement, which is estimated to be approximately a factor of 4 for single-organ imaging. Thus, quantification of liver segmental heterogeneity may become reliable on EXPLORER. Equivalently, the whole-liver ROI noise level may also be reduced

Table 6. Normalized absolute Bias, SD and RMSE of a typical kinetic parameter set (population means) estimated by the optimization-derived DBIF model with k_a freely estimated or fixed at its true value.

	Free k_a			Fixed k_a		
	Bias (%)	SD (%)	RMSE (%)	Bias (%)	SD (%)	RMSE (%)
K_1	3.2	10.8	11.3	0.3	3.0	3.0
k_2	3.5	11.6	12.1	0.4	3.4	3.4
k_3	5.0	19.7	20.6	17.7	17.9	17.9
k_4	8.1	44.0	45.2	4.6	41.6	42.1
K_i	4.5	18.3	19.1	1.7	16.6	16.7
v_b	71.8	206.5	158.1	47.9	116.9	91.0
k_a	3.9	16.2	16.8	/	/	/
f_A	38.3	121.9	93.6	40.0	106.0	81.4

from current $S_c = 0.3$ to $S_c = 0.15$ if EXPLORER is used. The resulting bias and SD of K_1 were 1.4% and 6.5%, respectively, according to our simulation study using $S_c = 0.15$.

This study has limitations. While the Monte Carlo-based 1D computer simulation approach used in this work is not different from other studies of kinetic modeling (e.g. Wu and Carson (2002)), the approach simulated the noise of TACs in the temporal domain but neglected potential spatial correlations of the noise. A fully 4D Monte Carlo simulation (e.g. by GATE) can be more realistic, though we do not expect that it would result in a significant difference in TAC noise modeling. The nonlinear least-square fitting in this work was solved by the classic Levenberg–Marquardt optimization algorithm, which only finds local solutions. Our preliminary study of multi-initialization indicated that a better optimization search could be beneficial. Thus, our future work will include the development of an improved optimization algorithm for this application. In addition, the model needs to be further modified if kinetic parameters (e.g. v_b) other than K_1 and K_i are of interest. A possible solution could be to include the gut compartment in a way similar to Garbarino *et al* (2015).

5. Conclusion

This paper has conducted both theoretical analysis of structural identifiability and computer study of practical identifiability for the optimization-derived DBIF model in dynamic PET of liver inflammation. The theoretical analysis suggests that the parameters of the new model are identifiable but subject to local solutions. The simulation results have shown that the estimation of vascular kinetic parameters (v_b and f_A) suffer from high variation. However, FDG K_1 can be reliably estimated in the new optimization-derived DBIF model. The bias of K_1 by the new model is approximately 3% and the standard deviation is about 11% at the whole-liver ROI noise level. The estimated values of K_1 are also highly correlated with the original K_1 values ($r = 0.92$). The correlation between liver FDG K_1 by the new model and histological inflammation score is robust to noise interference. These results suggest that liver FDG K_1 quantification is reliable for clinical use to assess liver inflammation at the whole-liver ROI level. Future work will include further development of the DBIF modeling and optimization approaches and use of EXPLORER for reduced bias and variance in K_1 .

Acknowledgments

The authors thank the anonymous reviewers for their helpful comments. The work of G Wang was supported in part by the UC Davis Comprehensive Cancer Center under NIH Grant P30 CA093373 and K12 Dean's Scholar Award.

Appendix

A.1. Structural identifiability of single-input kinetic model

Substituting equations (4)–(9) into equation (20), we have

$$D(s) = s^2 + \alpha_1 \cdot s + \alpha_0, \quad (\text{A.1})$$

$$N(s) = \beta_2 \cdot s^2 + \beta_1 \cdot s + \beta_0, \quad (\text{A.2})$$

where the coefficients are defined by

$$\alpha_1 = k_2 + k_3 + k_4, \quad (\text{A.3})$$

$$\alpha_0 = k_2 k_4, \quad (\text{A.4})$$

$$\beta_2 = v_b, \quad (\text{A.5})$$

$$\beta_1 = (1 - v_b)K_1 + v_b(k_2 + k_3 + k_4), \quad (\text{A.6})$$

$$\beta_0 = (1 - v_b)K_1(k_3 + k_4) + v_b k_2 k_4. \quad (\text{A.7})$$

Using the equation set $\alpha_i = D_i$ and $\beta_i = N_i$, we can obtain a unique solution for θ after some algebraic operations:

$$v_b = N_2, \quad (\text{A.8})$$

$$K_1 = \frac{N_1 - v_b D_1}{1 - v_b}, \quad (\text{A.9})$$

$$k_2 = D_1 - \frac{(N_0 - v_b D_0)}{(1 - v_b)K_1}, \quad (\text{A.10})$$

$$k_4 = \frac{D_0}{k_2}, \quad (\text{A.11})$$

$$k_3 = D_1 - k_2 - k_4. \quad (\text{A.12})$$

Therefore, the traditional SBIF three-compartmental model structure is globally identifiable in the parameter space.

A.2. Derivation of the structural identifiability of dual-input kinetic modeling

Similarly, for the optimization-derived DBIF model, the numerator and denominator of the transfer function $\Phi(s)$ are given by

$$D(s) = s^3 + (k_a + \alpha_1) \cdot s^2 + (k_a \alpha_1 + \alpha_0) \cdot s + k_a \alpha_0, \quad (\text{A.13})$$

$$N(s) = \beta_2 f_A \cdot s^3 + (k_a \beta_2 + f_A \beta_1) \cdot s^2 + (k_a \beta_1 + f_A \beta_0) \cdot s + k_a \beta_0 \quad (\text{A.14})$$

where $\{\alpha_i, \beta_i\}$ are defined by equations (A.3)–(A.7). The equation set to determine θ is:

$$k_a + \alpha_1 = D_2, \quad (\text{A.15})$$

$$k_a \alpha_1 + \alpha_0 = D_1, \quad (\text{A.16})$$

$$k_a \alpha_0 = D_0, \quad (\text{A.17})$$

$$\beta_2 f_A = N_3, \quad (\text{A.18})$$

$$k_a \beta_2 + f_A \beta_1 = N_2, \quad (\text{A.19})$$

$$k_a \beta_1 + f_A \beta_0 = N_1, \quad (\text{A.20})$$

$$k_a \beta_0 = N_0. \quad (\text{A.21})$$

Using equations (A.15)–(A.17), we obtain equation (26) for k_a . Using equations (A.18)–(A.21), we obtain equation (27) for f_A .

ORCID iDs

Guobao Wang  <https://orcid.org/0000-0001-6526-1533>

References

- Anderson D 1983 *Compartmental Modeling and Tracer Kinetics (Lecture Notes in Biomathematics)* (Berlin: Springer)
- Badawi R D *et al* 2019 First human imaging studies with the EXPLORER total-body PET scanner *J. Nucl. Med.* **60** 299–303
- Bellman R and Astrom K J 1970 On structural identifiability *Math. Biosci.* **7** 329–39
- Brix G, Ziegler S I, Bellemann M E, Doll J, Schosser R, Lucht R, Krieter H, Nosske D and Haberkorn U 2001 Quantification of [F-18]FDG uptake in the normal liver using dynamic PET: impact and modeling of the dual hepatic blood supply *J. Nucl. Med.* **42** 1265–73
- Carson R E, Yan Y, Daubewitherspoon M E, Freedman N, Bacharach S L and Herscovitch P 1993 An approximation formula for the variance of PET region-of-interest values *IEEE Trans. Med. Imaging* **12** 240–50

- Cherry S R, Badawi R D, Karp J S, Moses W W, Price P and Jones T 2017 Total-body imaging: transforming the role of positron emission tomography *Sci. Transl. Med.* **9** eaaf6169
- Cherry S R, Jones T, Karp J S, Qi J Y, Moses W W and Badawi R D 2018 Total-body PET: maximizing sensitivity to create new opportunities for clinical research and patient care *J. Nucl. Med.* **59** 3–12
- Delbary F, Garbarino S and Vivaldi V 2010 Compartmental analysis of dynamic nuclear medicine data: models and identifiability *Inverse Problems* **32** 125010
- Doot R K, Muzi M, Peterson L M, Schubert E K, Gralow J R, Specht J M and Mankoff D A 2010 Kinetic analysis of ^{18}F -fluoride PET images of breast cancer bone metastases *J. Nucl. Med.* **51** 521–7
- El Fakhri G, Kardan A, Sitek A, Dorbala S, Abi-Hatem N, Lahoud Y, Fischman A, Coughlan M, Yasuda T and Di Carli M F 2009 Reproducibility and accuracy of quantitative myocardial blood flow assessment with ^{82}Rb PET: comparison with ^{13}N -ammonia PET *J. Nucl. Med.* **50** 1062–71
- Garbarino S, Vivaldi V, Delbary F, Caviglia G, Piana M, Marini C, Capitanio S, Calamia I, Buschiazio A and Sambuceti G 2015 A new compartmental method for the analysis of liver FDG kinetics in small animal models *EJNMMI Res.* **5** 107
- Gunn R 1996 Mathematical modelling and identifiability applied to positron emission tomography data *PhD Thesis* University of Warwick
- Hu J, Panin V, Smith A M, Vijay Shah W H, Kehren F and Casey M 2017 Clinical whole body CBM parametric PET with flexible scan modes *Conf. Record of IEEE Nuclear Science Symp. and Medical Imaging Conf.*
- Karakatsanis N A, Lodge M A, Casey M E, Zaidi H and Rahmim A 2014 Impact of acquisition time-window on clinical whole-body PET parametric imaging *IEEE Nuclear Science Symp. and Medical Imaging Conf.*
- Karakatsanis N A, Lodge M A, Tahari A K, Zhou Y, Wahl R L and Rahmim A 2013a Dynamic whole-body PET parametric imaging: I. Concept, acquisition protocol optimization and clinical application *Phys. Med. Biol.* **58** 7391–418
- Karakatsanis N A, Lodge M A, Zhou Y, Wahl R L and Rahmim A 2013b Dynamic whole-body PET parametric imaging: II. Task-oriented statistical estimation *Phys. Med. Biol.* **58** 7419–45
- Karakatsanis N A, Zhou Y, Lodge M A, Casey M E, Wahl R L, Zaidi H and Rahmim A 2015 Generalized whole-body Patlak parametric imaging for enhanced quantification in clinical PET *Phys. Med. Biol.* **60** 8643–73
- Keiding S 2012 Bringing physiology into PET of the liver *J. Nucl. Med.* **53** 425–33
- Keramida G, Potts J, Bush J, Dizdarevic S and Peters A M 2014 Hepatic steatosis is associated with increased hepatic FDG uptake *Eur. J. Radiol.* **83** 751–5
- Keramida G, Potts J, Bush J, Verma S, Dizdarevic S and Peters A M 2014 Accumulation of F-18-FDG in the liver in hepatic steatosis *Am. J. Roentgenol.* **203** 643–8
- Kudomi N et al 2009 Non-invasive estimation of hepatic glucose uptake from [^{18}F]FDG PET images using tissue-derived input functions *Eur. J. Nucl. Med. Mol. Imaging* **36** 2014–26
- Lee S S and Park S H 2014 Radiologic evaluation of nonalcoholic fatty liver disease *World J. Gastroenterol.* **20** 7392–402
- Mankoff D, Muzi M and Zaidi H 2006 Quantitative analysis in nuclear oncologic imaging *Quantitative Analysis in Nuclear Medicine Imaging* (New York: Springer) pp 494–536
- Mankoff D A, Shields A F, Graham M M, Link J M, Eary J F and Krohn K A 1998 Kinetic analysis of 2-[carbon-11]thymidine PET imaging studies: compartmental model and mathematical analysis *J. Nucl. Med.* **39** 1043–55
- Messa C, Choi Y, Hoh C K, Jacobs E L, Gaspy J A, Rege S, Nitzsche E, Huang S C, Phelps M E and Hawkins R A 1992 Quantification of glucose utilization in liver metastases: parametric imaging of FDG uptake with PET *J. Comput. Assist. Tomogr.* **16** 684–9
- Miao H, Dykes C, Demeter L M, Cavanaugh J, Park S Y, Perelson A S and Wu H 2008 Modeling and estimation of kinetic parameters and replicative fitness of HIV-1 from flow-cytometry-based growth competition experiments *Bull. Math. Biol.* **70** 1749–71
- Miao H, Xia X, Perelson A S and Wu H 2011 On identifiability of nonlinear ODE models and applications in viral dynamics *SIAM Rev. Soc. Ind. Appl. Math.* **53** 3–39
- Michelotti G A, Machado M V and Diehl A M 2013 NAFLD, NASH and liver cancer *Nat. Rev. Gastroenterol. Hepatol.* **10** 656–65
- Miyazawa H, Osmont A, Petit-Taboue M C, Tillet I, Traversi J M, Young A R, Barre L, MacKenzie E T and Baron J C 1993 Determination of ^{18}F -fluoro-2-deoxy-d-glucose rate constants in the anesthetized baboon brain with dynamic positron tomography *J. Neurosci. Methods* **50** 263–72
- Mourik J E, Lubberink M, Klumpers U M, Comans E F, Lammertsma A A and Boellaard R 2008 Partial volume corrected image derived input functions for dynamic PET brain studies: methodology and validation for [^{11}C]flumazenil *NeuroImage* **39** 1041–50
- Munk O L, Bass L, Roelsgaard K, Bender D, Hansen S B and Keiding S 2001 Liver kinetics of glucose analogs measured in pigs by PET: importance of dual-input blood sampling *J. Nucl. Med.* **42** 795–801
- Musso G, Gambino R, Cassader M and Pagano G 2011 Meta-analysis: natural history of non-alcoholic fatty liver disease (NAFLD) and diagnostic accuracy of non-invasive tests for liver disease severity *Ann. Med.* **43** 617–49
- Muzi M, Mankoff D A, Grierson J R, Wells J M, Vesselle H and Krohn K A 2005 Kinetic modeling of 3'-deoxy-3'-fluorothymidine in somatic tumors: mathematical studies *J. Nucl. Med.* **46** 371–80
- Muzi M, Spence A M, O'Sullivan F, Mankoff D A, Wells J M, Grierson J R, Link J M and Krohn K A 2006 Kinetic analysis of 3'-deoxy-3'-18F-fluorothymidine in patients with gliomas *J. Nucl. Med.* **47** 1612–21
- Okazumi S, Isono K, Enomoto K, Kikuchi T, Ozaki M, Yamamoto H, Hayashi H, Asano T and Ryu M 1992 Evaluation of liver tumors using fluorine-18-fluorodeoxyglucose PET: characterization of tumor and assessment of effect of treatment *J. Nucl. Med.* **33** 333–9
- Oppenheim A V, Willsky A S and Nawab S H 1996 *Signals and Systems* 2nd edn (Upper Saddle River, NJ: Prentice-Hall)
- Poon J K et al 2012 Optimal whole-body PET scanner configurations for different volumes of LSO scintillator: a simulation study solution *Phys. Med. Biol.* **57** 4077–94
- Sarkar S, Corwin M, Olson K, Stewart S, Johnson C R, Badawi R and Wang G B 2017 4D dynamic FDG-PET correlates with hepatic inflammation and steatosis in patients with non-alcoholic steatohepatitis *Hepatology* **66** 107a–8a (abstract)
- Sarkar S, Corwin M, Olson K, Stewart S, Liu C, Badawi R and Wang G 2019 Pilot study to diagnose non-alcoholic steatohepatitis with dynamic ^{18}F -fluorodeoxyglucose positron emission tomography *Am. J. Roentgenol.* **212** 529–37
- Tsien H 1954 *Engineering Cybernetics* (New York: McGraw-Hill)
- Wang G, Corwin M, Olson K, Stewart S, Zha C, Badawi R and Sarkar S 2017 Dynamic FDG-PET study of liver inflammation in non-alcoholic fatty liver disease *J. Hepatol.* **66** S592
- Wang G, Corwin M T, Olson K A, Badawi R D and Sarkar S 2018 Dynamic PET of human liver inflammation: impact of kinetic modeling with optimization-derived dual-blood input function *Phys. Med. Biol.* **63** 155004
- Winterdahl M, Munk O L, Sorensen M, Mortensen F V and Keiding S 2011 Hepatic blood perfusion measured by 3 min dynamic F-18-FDG PET in pigs *J. Nucl. Med.* **52** 1119–24
- Wree A, Broderick L, Canbay A, Hoffman H M and Feldstein A E 2013 From NAFLD to NASH to cirrhosis-new insights into disease mechanisms *Nat. Rev. Gastroenterol. Hepatol.* **10** 627–36

- Wu Y J and Carson R E 2002 Noise reduction in the simplified reference tissue model for neuroreceptor functional imaging *J. Cerebral Blood Flow Metab.* **22** 1440–52
- Xie L, Yui J, Hatori A, Yamasaki T, Kumata K, Wakizaka H, Yoshida Y, Fujinaga M, Kawamura K and Zhang M R 2012 Translocator protein (18 kDa), a potential molecular imaging biomarker for non-invasively distinguishing non-alcoholic fatty liver disease *J. Hepatol.* **57** 1076–82
- Zhang X Z, Zhou J, Cherry S R, Badawi R D and Qi J Y 2017 Quantitative image reconstruction for total-body PET imaging using the 2 m long explorer scanner *Phys. Med. Biol.* **62** 2465–85